Molecular dynamics simulations of cascades in strained carbide inclusions embedded in alpha-iron

Henriksson, K. O. E.

2015-11

Henriksson , K O E & Nordlund , K 2015 , ' Molecular dynamics simulations of cascades in strained carbide inclusions embedded in alpha-iron ' , AIP Advances , vol. 5 , no. 11 , 117152 . https://doi.org/10.1063/1.4936883

http://hdl.handle.net/10138/175077
https://doi.org/10.1063/1.4936883

Molecular dynamics simulations of cascades in strained carbide inclusions embedded in α–iron

K. O. E. Henriksson and K. Nordlund

Citation: AIP Advances **5**, 117152 (2015); doi: 10.1063/1.4936883
View online: http://dx.doi.org/10.1063/1.4936883
View Table of Contents: http://aip.scitation.org/toc/adv/5/11
Published by the American Institute of Physics

Molecular dynamics simulations of cascades in strained carbide inclusions embedded in α-iron

K. O. E. Henriksson[a] and K. Nordlund
Department of Physics, P.O. Box 43, FI-00014 University of Helsinki, Finland

(Received 30 September 2015; accepted 16 November 2015; published online 30 November 2015)

The effect of strain on the amount of point defects created in Fe and Cr carbide inclusions embedded in ferrite has been investigated. The spherical carbide inclusions consisted of either Fe_3C or $Cr_{23}C_6$. Recoil energies from 100 eV to 3 keV and strains from −0.15 (compressive) to 0.01 (tensile) were used. The overall tendency is that the number of point defects — such as antisites, vacancy and interstitials — inside the carbide is lowered when the strain grows more negative (compressive). Outside the carbides, the number of defects is markedly higher for strongly compressive strains than for *e.g.* zero strain, especially at high energies. [http://dx.doi.org/10.1063/1.4936883]

I. INTRODUCTION

Cementite Fe_3C and $Cr_{23}C_6$ are among the principal pure carbides that can occur in model stainless steels (Fe-Cr-C) based on ferrite (α-iron, body-centered cubic (BCC) crystal structure) (see *e.g.* Ref. 1). Martensitic/ferritic stainless steels can be used as construction materials in nuclear applications, where they are subjected to *e.g.* neutron irradiation (see *e.g.* Refs. 2–5). Atoms knocked from their lattice sites by energetic neutrons create cascades in the material, leading to the formation of defects. In a metal containing carbide inclusions, there are three distinct regions where point defects can be created: (i) inside the carbide, (ii) at the interface between carbide and metal, and (iii) in the host metal. In order to minimize defect production one would need to minimize defect production in all three regions. Barring any alloying of or other changes to the metal, the carbides can more easily be manipulated — at least computationally — to achieve such a goal. One way to manipulate the carbides would be to subject them to a non-zero strain. This is easily explored in a computational study.

In the present work, a recent semiempirical potential for the Fe-Cr-C system[6] is used to explore this idea. In the following section the technical details of the work is laid out, with results and discussion following in Sec. III, and conclusions in Sec. IV.

II. METHODS

A. Making of initial cells

The cells of Fe_3C and $Cr_{23}C_6$ were obtained from the density functional theory results presented in Ref. 7. Large cells of ferrite and the carbides Fe_3C and $Cr_{23}C_6$ — the latter ones with Cartesian border lengths around 100 Å — were relaxed at 300 K and 0 GPa using the Berendsen thermostat and barostat.[8] For Fe the simulation cell was cubic, with a side lenght of $38a$, a = 2.89 Å being the lattice parameter. After relaxation a sphere of radius 20.5 Å was cut out to make room for a carbide inclusion. The atom closest to to the origin (0,0,0) — with position $\mathbf{r}_0^{\mathrm{Fe}}$ — was selected and all atoms inside a sphere centered on this atom were removed. All molecular dynamics simulations were carried out using the code PARCAS[9–12] and bond-order type interatomic potentials for Fe-Cr-C taken from Ref. 6.

[a]Electronic mail: krister.henriksson@helsinki.fi

Carbide inclusions with different strains were prepared by isotropically straining the large carbide cells. This was done by transforming original positions $\mathbf{x}$ to $\mathbf{x}' = (1 + \varepsilon)\mathbf{x}$. The strain ε was varied from −0.15 to 0.15 with different increments. Spheres of radius 20 Å were extracted from these strained carbide cells, by first locating the atom closest to the origin (0,0,0) — the center of the carbide, with position $\mathbf{r}_0^{(c)}$ — and then extracting all atoms situated inside a sphere centered on this position. The carbide sphere was then combined with the Fe host containing the corresponding spherical cavity, such that the carbide center $\mathbf{r}_0^{(c)}$ coincided with the center $\mathbf{r}_0^{(Fe)}$ of the cavity. This guarantees that the interface region is as uniform as possible in all directions. Each complete cell — Fe host with strained carbide inclusion — was carefully relaxed at 300 K and 0 GPa for 50 ps to prepare them for the cascade simulations.

Upon relaxation it became evident that strains of $\varepsilon \geq 0.03$ makes the carbide inclusions only partially attach to the spherical cavity inside the Fe host. This enables the inclusion to relax to a less strained state, leaving empty space in between carbide and host lattice, thereby rendering the complete cell inadequate for cascade simulation. Results for these cases are therefore not presented in this work.

B. Cascade simulations

The samples used for cascade simulations were periodic. Recoil positions were randomly selected inside a sphere of radius 10 Å centered on the carbide inclusion. A set of N_r recoil positions $\mathbf{x}_i^{(r)}$ were generated. In order to obtain comparable results, this set of recoil positions was used for all strain states and all recoil energies. The recoil energies varied between 100 eV and 3 keV. For each recoil energy and strain level, $N_r = 50$ recoil simulations were carried out, each using a simulation time of 50 ps. Berendsen temperature control was applied in border of thickness regions 6 Å, with a target temperature of 300 K. No pressure control was used.

Before starting a recoil simulation, the cell was shifted in all Cartesian directions (periodic boundary conditions were enforced) so that the initial recoil position was at the very center of the cell. The actual recoiling atom was the metal atom (Fe or Cr) closest to this position.

Electronic stopping by Ziegler *et al.*,[13] obtained from the ZBL96 code developed in our laboratory, was used on all atoms having an energy of 5 eV or more.

C. Analysis methods

A Wigner-Seitz[14] (WS) cell analysis was used to find vacancies (empty WS cells) and interstitials (WS cells containing two or more atoms) in the relaxed samples. The degree of clustering of the defects was also analyzed. Two vacancies (or interstitials) were considered to form a cluster if they were separated by a distance $r \leq r_c$. The chosen value was $r_c = 2.7$ Å, which is enough to ensure that first neighbor vacancies in ferrite are clustered.

The fraction of defects of a certain type (vacancy or interstitial) which are located in a cluster of size N or larger is calculated as

$$f_c(N) = \left(\sum_{i=N}^{M} i \times N_c(i) \right) / N_d, \tag{1}$$

where M is the number of defects in the largest cluster, $N_c(i)$ is the number of clusters containing i defects, and $N_d = \sum_{i=1}^{M} i \times N_c(i)$ is the total number of individual defects. If nothing else is specified, a value of $N = 2$ was used.

Defects were also analyzed for their distance to the carbide center. For each energy and strain ε, the radial distances for defects in all cascade simulations were collected. The subsequent histograms displays a yield density, defined as

$$Y_X(r_i) = \frac{N_X(r_i)}{N_{\text{rec}} \cdot V_{\text{shell}}(r_i)}, \tag{2}$$

where X is the defect type, r_i is the radial distance to the center of shell i, $N_X(r_i)$ is the number of defects of type X inside shell i, N_{rec} is the number of recoils (equals the number of cascades), and

$V_{\text{shell}}(r_i)$ is the volume of the spherical shell centered on radial distance r_i. In all cases a shell width of 5 Å was used.

The strain state of the carbides after relaxation and after each cascade was calculated using the distances $r_i^{(c)}, i \geq 1$ of the C atoms to the carbide center $\mathbf{r}_0^{(c)}$. All distances larger than the radius 20 Å were ignored. From the pristine cells one has $r_i^{(c)}(\text{before relaxation})(\varepsilon) \equiv (1+\varepsilon) r_i^{(c)}(\text{original})(0)$ where ε is the strain applied to the original positions. From the relaxed and post-cascade cells one has $r_i^{(c)}(\text{after})(\varepsilon') \equiv (1+\varepsilon') r_i^{(c)}(\text{original})(0)$, where ε' can be solved for using known positions and the strain ε applied to the initial cell before any relaxation of cascade damage.

III. RESULTS AND DISCUSSION

A. Relaxed cells

Cross-sections of the cells after relaxation and a 3 keV cascade are shown in Fig. 1. The cells containing the largest amount of vacancies were chosen for the visualization of the damage. For

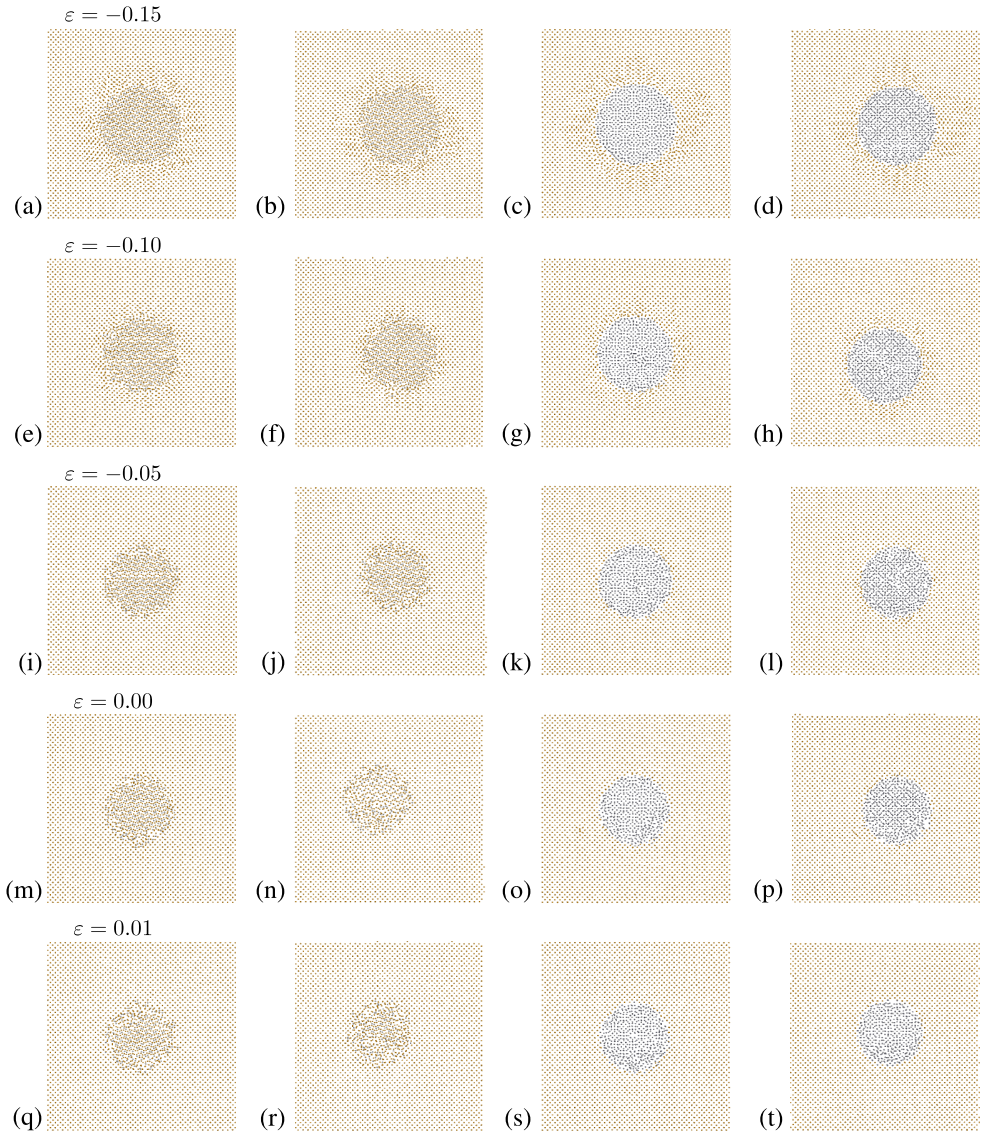

FIG. 1. Cross-sections of (a,e,i,m,q,c,g,k,o,s) relaxed (first and third figure column) and (b,f,j,n,r,d,h,l,p,t) damaged (second and fourth figure column) cells. First and second column is for Fe_3C inclusions and third and fourth is for $Cr_{23}C_6$ inclusions.

TABLE I. Relationship between initial strain and strain after relaxation for the carbide inclusions.

Carbide type	Initial strain ε	Strain after relaxation ε'
Fe	−0.15	−0.151 ± 0.009
Fe	−0.10	−0.099 ± 0.010
Fe	−0.05	−0.059 ± 0.011
Fe	0.00	−0.015 ± 0.012
Fe	0.01	−0.008 ± 0.013
Cr	−0.15	−0.151 ± 0.005
Cr	−0.10	−0.101 ± 0.005
Cr	−0.05	−0.051 ± 0.007
Cr	0.00	−0.013 ± 0.006
Cr	0.01	−0.009 ± 0.006

the largest compressive strains, the local metal lattice is highly strained, but the carbide inclusion maintains a high degree of crystalline order. For lower strains the inclusion can expand more. The more positive the strain, the fewer number of atoms there is in the carbide with the spherical radius of 20 Å. The Fe_3C inclusions appear to suffer more damage than the $Cr_{23}C_6$ inclusions, a fact which is verified by the numerical results, which are plotted in Section III E.

As can be seen from the figure, relaxation of carbides already creates defects in the cells. The defects are located inside and outside the carbides as well as at the carbide-host interfaces.

For $\varepsilon \geq 0$ the number of vacancies is 300 − 400. Between $\varepsilon = -0.15$ and $\varepsilon = -0.05$ the number N_V of vacancies scales linearly with the strain, with $N_V\,(\varepsilon = -0.15) \sim 2500$ and $N_V\,(\varepsilon = -0.05) \sim 400$. The number of interstitials equals the number of vacancies. The peak of the distributions for vacancies move outward from 10 Å to 15 Å with increasing strain, going from $\varepsilon = -0.15$ to $\varepsilon = 0.01$. The peak of the distributions for interstitials move outward from 25 Å to 20 Å with increasing strain.

The strain states of the carbides in the relaxed cells are shown in Table I. The results show that the strain does not change very much in the case of compressive strains. The tensile strains, on the other hand, decreases and become more compressive.

B. Strain in damaged carbide inclusions

The strain states of the carbides in the post-cascade cells are shown in Table II. The results show that the strain is similar to the pre-cascade strain, shown in Table I.

TABLE II. Relationship between initial strain and strain after cascade formation for the carbide inclusions. The uncertainties are of order $\lesssim 10^{-4}$ and therefore not shown.

Carbide type	Initial strain ε	Strain after cascades ε'
Fe	−0.15	−0.152
Fe	−0.10	−0.100
Fe	−0.05	−0.060
Fe	0.00	−0.017
Fe	0.01	−0.009
Cr	−0.15	−0.152
Cr	−0.10	−0.099
Cr	−0.05	−0.051
Cr	0.00	−0.013
Cr	0.01	−0.006

C. Cascade size

The size of the cascade occurring in the simulations can be determined by *e.g.* inspecting the time evolution of the defects and the size of the region in which they form. With the primary knock-on atom known, the radial distance of defects to this initial cascade center can be calculated. With approximate spherical symmetry, the cascade size can be estimated as spherical with a radius given by the average radial distance of defects to the initial cascade center.

This method relies on the existence of a single cascade, not multiple cascades. The latter requires higher energies than used in the present studies, so this complication does not arise. The occurrence of *e.g.* long replacement collisions extending beyond the primary cascade region would also render the present method of determining cascade sizes less than useful. However, visual inspection of the analyzed runs shows that no such phenomena occurred.

The maximum anbd average radial distances of vacancies and interstitials from the initial cascade center are shown in Fig. 2(a)-2(b) and 2(c)-2(d), respectively. Maximum distances are about 40 Å (for interstitials) or less, and these occur inside 1 ps after initiation of cascade. At the end of the runs the maximum distance is about 30 Å (for interstitials) or less. The average radial distance at the end of the runs is 25 Å (for interstitials) or less, with local maxima below this value occurring inside 1 ps after initiation of cascade. The stabilized values at the end of the runs mostly follow the strain: the largest compressive strain shows the largest average distance, and the most tensile strain show the smallest average distance. With the radius of the inclusions being 20 Å, this indicates that the bulk of the cascades is mostly inside the inclusions, but they do reach beyond the interface and in to the host matrix.

D. Antisites

The number N_{AS} of antisites formed in the cascades is shown in Fig. 3. The M_{AS} increases with energy for all strains ε. In general, $\varepsilon < 0$ produce less antisites than $\varepsilon \geq 0$.

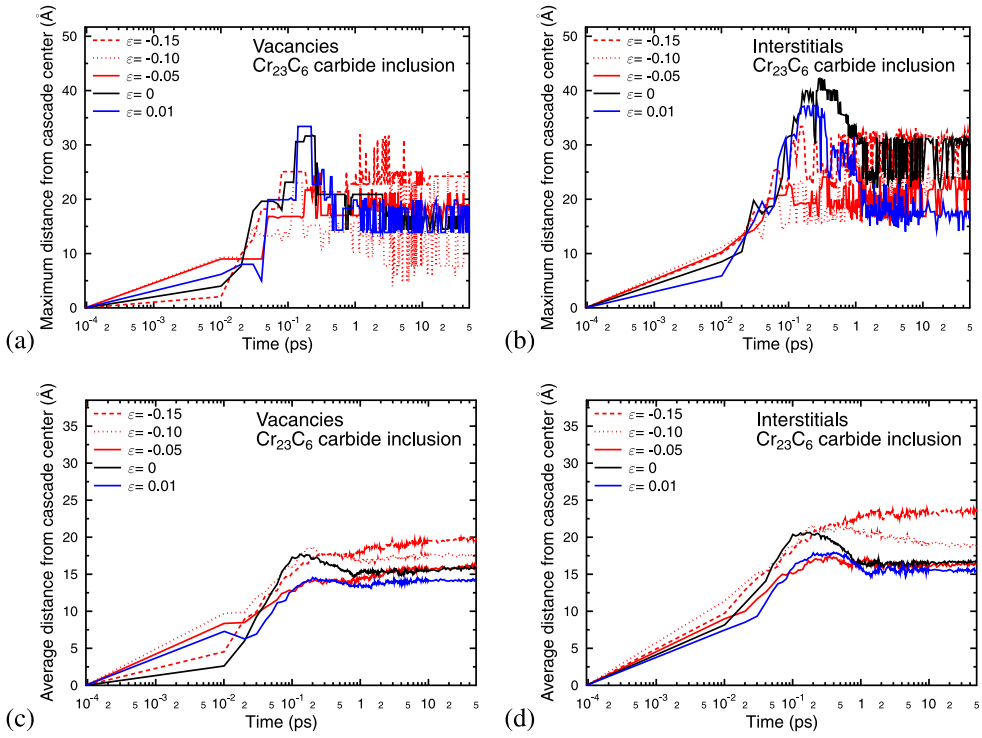

FIG. 2. Maximum (a)-(b) and average (c)-(d) radial distance of defects from cascade center as a function of time for the case of 3 keV cascade in a $Cr_{23}C_6$ inclusion. The run producing the larget amount of defects for a given strain was selected for that strain.

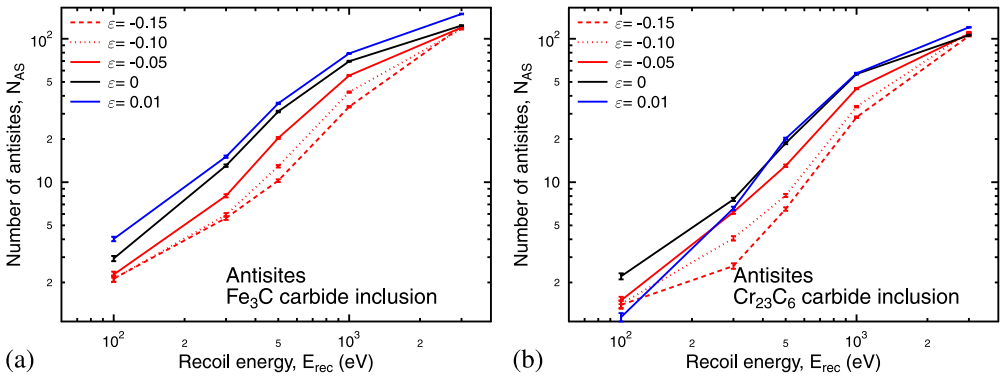

FIG. 3. (a)-(b): Number of antisites as a function of recoil energy.

The radial distributions of antisites are shown in Fig. 4 for Fe_3C. For recoil energies above 300 eV (inclusive) $\varepsilon \geq 0$ have clearly defined peaks between 10 and 20 Å. In other words, already small energies are enough to cause species exchanges for relatively weakly strained carbides, with the changes limited to inside the carbides. Clear peaks for all of the cases $\varepsilon < 0$ only appear at the highest energy 3 keV. For highly strained carbides species exchanges preferably stay close to the carbide center at low and moderate energies. At higher energies, effects are increasingly present at the carbide-host interface and outside the carbide. This might simply be caused by the higher energy deposition working in conjunction with strain-release, effectively mixing up the interface.

E. Vacancies and interstitials

The number of vacancies produced in the cascades is displayed in Fig. 5. The number of vacancies increases with energy for all strain levels ε. At intermediate energies the smallest strains $\varepsilon \geq 0$ tend to produce the largest numbers of defects. At the lowest and highest energies, the highest compression $\varepsilon = -0.15$ produces the most defects for both carbides.

The radial distributions of vacancies and interstitials in the case of Fe_3C are shown in Fig. 6 and Fig. 7, respectively. The results for $Cr_{23}C_6$ are similar and are hence not shown.

The vacancy distributions for all ε decrease with increasing radial distance for energies below 1 keV, indicating that vacancy defects are mainly inside the carbides at these energies, and close to the core. At the two highest energies of 1 and 3 keV peaks start to appear between 10 and 20 Å, and in the case of $\varepsilon < 0$ the location of the peaks are close to or at the carbide-host interface,

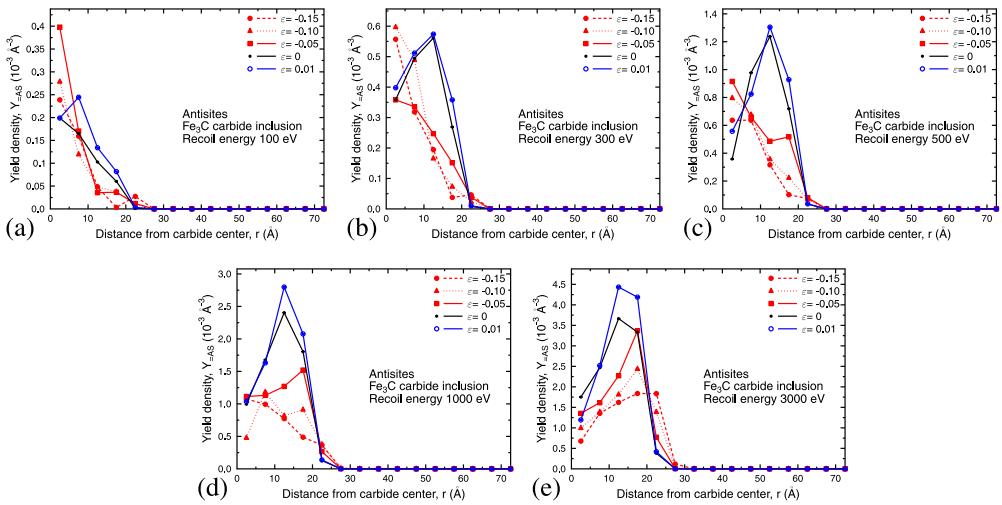

FIG. 4. Radial distribution of antisites for Fe_3 C, for (a) 100 eV, (b) 300 eV, (c) 500 eV, (d) 1 keV, and (e) 3 keV.

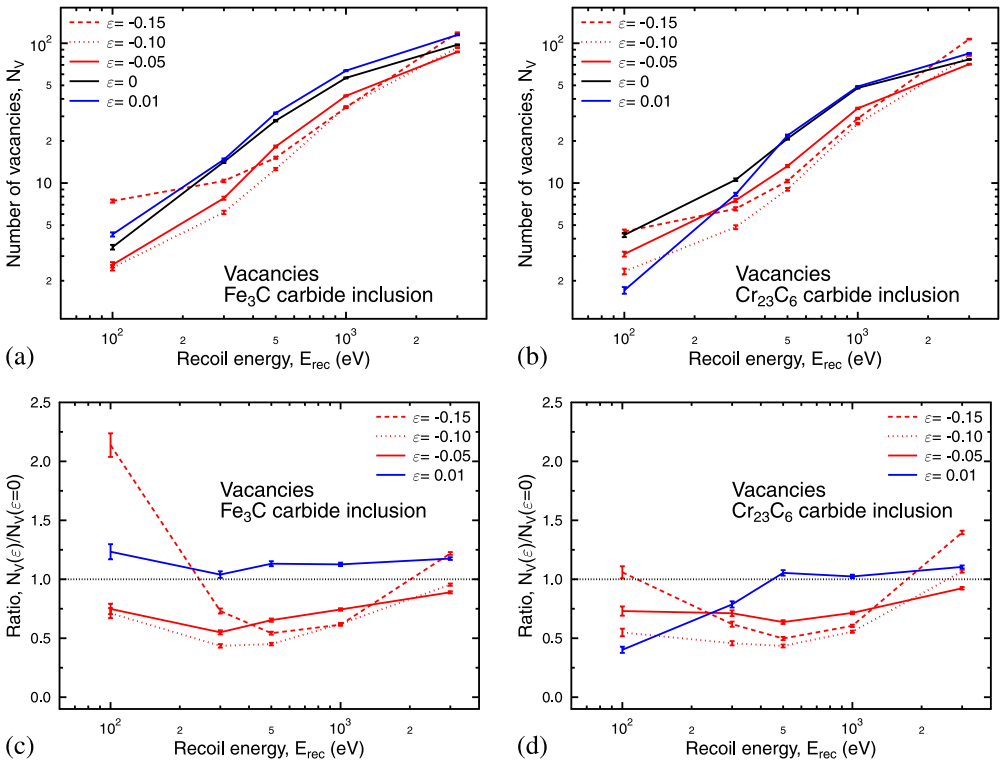

FIG. 5. (a)-(b): Number of vacancies as a function of recoil energy. Notice the different scales of the ordinates for the carbide types. (c)-(d): Ratio of vacancies as a function of recoil energy. The number of interstitials equals the number of vacancies.

with significant contributions also at $r > 20$ Å, *i.e.* outside the carbides. In other words, increasing energies puts the majority of vacancies (and interstitials, see below) further out from the core of the carbides, and increases their presence outside the carbide, in the strained bulk region. In addition, the higher the compression, the more significant the contribution, *e.g.* for $\varepsilon = -0.15$ the distribution of vacancies (and interstitials) survives further out and is more significant than for *e.g.* $\varepsilon = -0.10$. In comparison, for $\varepsilon \geq 0$ there are no significant contributions in this region. This indicates that high carbide compression — and high energy — is needed to produce vacancies (and interstitials) also outside the carbides, in the surrounding host lattice.

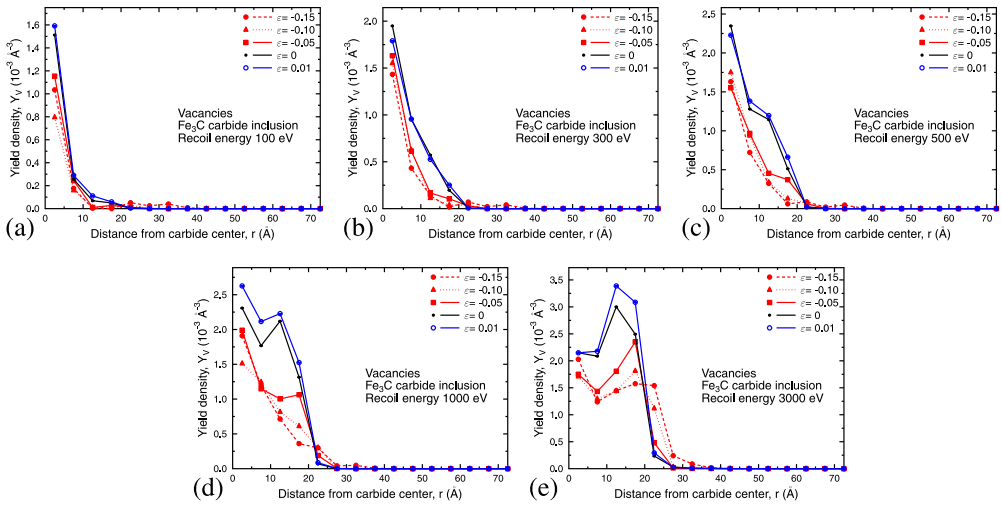

FIG. 6. Radial distribution of vacancies for Fe_3C, for (a) 100 eV, (b) 300 eV, (c) 500 eV, (d) 1 keV, and (e) 3 keV.

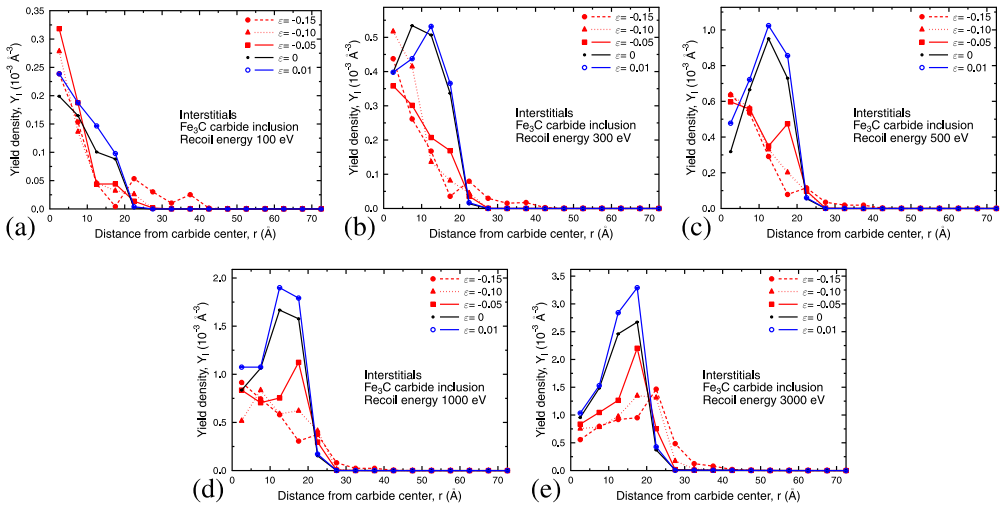

FIG. 7. Radial distribution of interstitials for Fe_3C, for (a) 100 eV, (b) 300 eV, (c) 500 eV, (d) 1 keV, and (e) 3 keV.

For interstitials and $\varepsilon \geq 0$ the peaks start to appear already at 300 eV, located between 10 and 20 Å. Comparing with vacancies, it can be seen that the peaks are further out than for vacancies, at energies up to 500 eV, inclusive. This indicates vacancies are produced further in and interstitials further out (following normal cascade dynamics[15]), the separating the separating "interface" moving outwards with increasing energy. For the highest energies the distributions are more overlapping.

For $\varepsilon < 0$ the vacancy peaks begin to appear weakly at 1 keV but are strongest at 3 keV, where they are located around 20 Å and further out. At the highest energy the situation for interstitials is very similar to that for vacancies, except that vacancies have a larger distribution than interstitials close to the center of the carbides. Comparing vacancies and interstitials at each energy, it can be seen that vacancy distributions are generally larger than those for interstitials at distances close to the carbide center, *i.e.* where the recoils are mostly started.

One consistent result for the point defects is that for $\varepsilon = -0.15$ a relatively large amount is produced at the lowest and/or highest recoil energies. The next highest compression $\varepsilon = -0.10$ and the other strains do not show this behavior. Comparing Fig. 6(a) and Fig. 7(a), it can be seen that for $\varepsilon = -0.15$ the defect distributions are more significant than for the other $\varepsilon < 0$ at $r \geq 20$ Å (this is best seen for interstitials, Fig. 7(a)). This indicates that a significant defect contribution is coming from the highly strained bulk region within $\sim 5 - 10$ Å of the interface. To verify this, animations were made of the cascades which create the largest number of vacancies or interstitials, for $\varepsilon = -0.15$ and for all energies investigated. Visual inspection of the animations for energies 300 eV to 3 keV clearly shows relaxation of some parts the strained host lattice, with crystalline order returning to regions previously under strain. At 100 eV this is not clearly visible. Alternatively, a zoom-in of the radial defect densities in Fig. 6(a) and Fig. 7(a), presented in Fig. 8(a) and 8(b), respectively, verifies that a large portion of the defects should nevertheless be in the highly strained part of the host lattice. However, it should be noted that $\varepsilon = -0.15$ does not always produce the largest numbers of defects. At intermediate energies, the defect numbers decrease when the strain goes from positive to more negative values. This indicates that the strain-release contribution to the defect numbers works in conjunction with the traditional damage production — inside or at the interface of the carbide — from the primary recoil itself. In this case annealing due to local melting of the carbide also makes a contribution to the defect numbers.

In summary, the reason for the "anomalously" high defect numbers for $\varepsilon = -0.15$, especially at low and high energies, must therefore be directly related to the existence of the highly strained host lattice, which is able to partially relax during a cascade event. The WS analysis code, which takes the undamaged highly strained lattice as a reference when looking for defects, will by necessity then find defects in or close to regions which have experienced large enough relaxations. It should be noted that the absolute number of defects is smaller in $Cr_{23}C_6$, see Fig. 5(b), but similar "anomalous" behavior is seen for $\varepsilon = -0.15$, part (d) of the figure. The explanations are similar as to the case for Fe_3C.

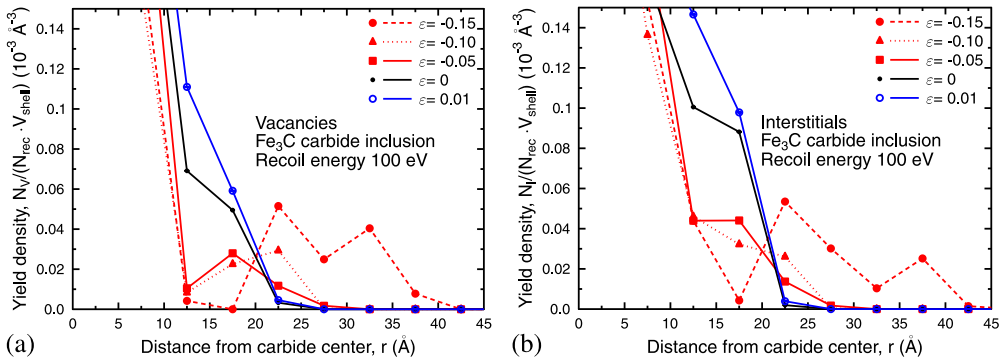

FIG. 8. Radial distribution of (a) vacancies and (b) interstitials for Fe_3C at 100 eV, partial enlargened plot based on data in Fig. 6(a) and Fig. 7(a).

F. Clustering of vacancies and interstitials

The fraction of vacancies and interstitials in clusters is shown in Fig. 9. The following observations can be made: (i) The clustering fraction increases with energy, but always stays below 0.7 – 0.8. (ii) For a given energy and strain, the clustering fraction of interstitials is generally lower than that for vacancies for both Fe and Cr. The only exception is 100 eV and $\varepsilon = 0$, where the order is reversed, but the absolute values are separated by ≤ 8 %. (iii) For a given defect type (vacancy or interstitial), energy and strain, the clustering fraction is generally smaller for Cr carbides than for Fe carbides. The only exception is 100 eV and $\varepsilon = -0.10$ and $\varepsilon = -0.05$, where the order is reversed, but the absolute values are separated by ≤ 13 %. (iv) For both carbides, negative strains (compression) $\varepsilon < 0$ in most cases produce lower clustering fractions than positive strains (tension) $\varepsilon > 0$. (v) The most negative strain $\varepsilon = -0.15$ produces the lowest clustering fraction for all energies except the lowest and sometimes the highest ones. This holds for both carbides.

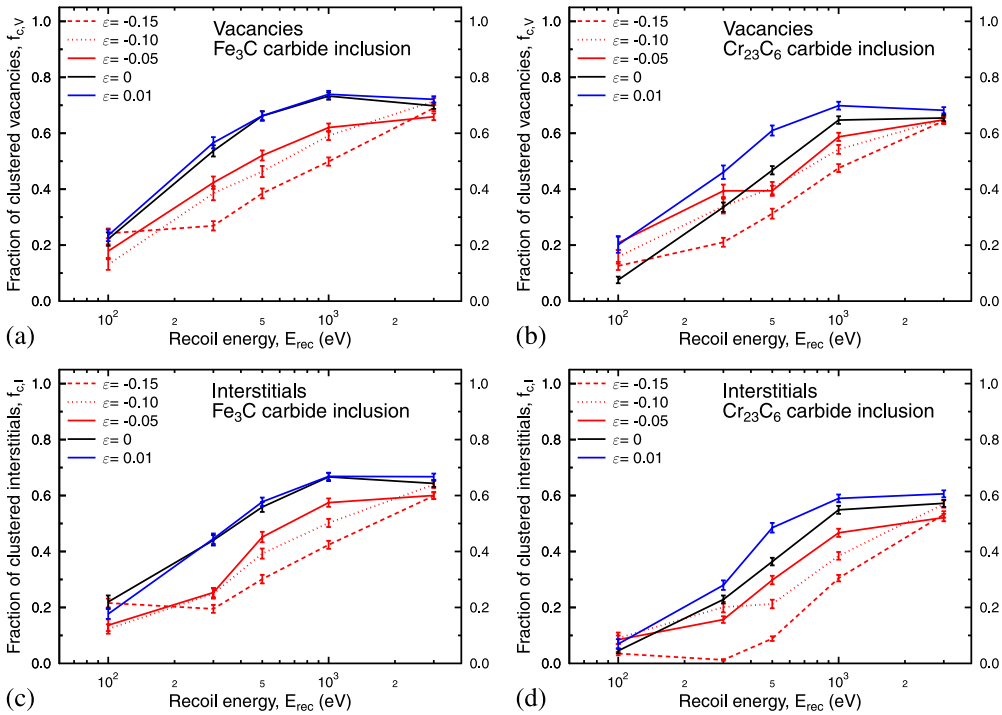

FIG. 9. Clustering fractions of (a-b) vacancies and (c-d) interstitials as a function of recoil energy.

IV. CONCLUSIONS

Molecular dynamics simulations of bulk cascades have been carried out for strained Fe_3C and $Cr_{23}C_6$ carbide inclusions embedded into ferrite. The number of point defects, such as antisites, vacancies, and interstitials, their clustering fraction, as well as radial distributions, have been calculated. The number of defects as well as the clustering fraction increases with energy. At intermediate energies the number of defects decreases when the strain ε is decreased towards high compressions. At lowest and highest energies the highest compression, $\varepsilon = -0.15$, tend to produce the largest amount of defects. Two types of defect production mechanisms seem to be involved: relaxation of the high-strain field in the host lattice closest to the carbide, and damage created by the cascade itself — primarily located inside or at the interface of the carbide (at higher energies).

ACKNOWLEDGMENTS

The molecular dynamics calculations presented in this article have been carried out in the CSC's computating environment. CSC is the Finnish IT center for science and is owned by the Ministry of Education. The research has been carried out with financial support from the Academy of Finland (contracts number 259249 and 264911).

[1] H. J. Goldschmidth, *Interstitial alloys* (Butterworths, London, U.K., 1967).
[2] G. R. Odette, M. J. Alinger, and B. D. Wirth, "Recent developments in irradiation-resistant steels," Annual Rev. Mater. Sci. **38**, 471–503 (2008).
[3] R. J. Kurtz, A. Alamo, E. Lucon, Q. Huang, S. Jitsukawa, A. Kimura, R. L. Klueh, G. R. Odette, C. Petersen, M. A. Sokolov, P. Spätig, and J. W. Rensman, "Recent progress toward development of reduced activation ferritic/martensitic steels for fusion structural applications," J. Nucl. Mater. **386-388**, 411–417 (2009).
[4] S. J. Zinkle and J. T. Busby, "Structural materials for fission and fusion energy," Materials Today **12**, 12–19 (2009).
[5] S. J. Zinkle and L. L. Snead, "Designing radiation resistance in materials for fusion energy," Annual Review of Materials Research **44**, 241–267 (2014), DOI: 10.1146/annurev-matsci-070813-113627.
[6] K. O. E. Henriksson, C. Björkas, and K. Nordlund, "Atomistic simulations of stainless steels: a many-body potential for the Fe-Cr-C system," J. Phys. Cond. Matter **25**, 445401 (2013).
[7] K. O. E. Henriksson, N. Sandberg, and J. Wallenius, "Carbides in stainless steels: Results from *ab initio* investigations," Appl. Phys. Lett. **93**, 191912 (2008).
[8] H. J. C. Berendsen, J. P. M. Postma, W. F. van Gunsteren, A. D. Nola, and J. R. Haak, "Molecular dynamics with coupling to an external bath," J. Chem. Phys. **81**, 3684 (1984).
[9] PARCAS computer code, K. Nordlund. The main principles of the molecular dynamics algorithm are presented in Refs. 10 and 11. The adaptive time step and electronic stopping algorithms are the same as in Ref. 12.
[10] K. Nordlund, M. Ghaly, R. S. Averback, M. Caturla, T. Diaz de la Rubia, and J. Tarus, "Defect production in collision cascades in elemental semiconductors and fcc metals," Phys. Rev. B **57**, 7556–7570 (1998).
[11] M. Ghaly, K. Nordlund, and R. S. Averback, "Molecular dynamics investigations of surface damage produced by kev self-bombardment of solids," Phil. Mag. A **79**, 795 (1999).
[12] K. Nordlund, "Molecular dynamics simulation of ion ranges in the 1 – 100 kev energy range," Comput. Mater. Sci. **3**, 448 (1995).
[13] J. F. Ziegler, J. P. Biersack, and U. Littmark, *The stopping and range of ions in matter* (Pergamon, New York, U.S.A., 1985).
[14] N. W. Ashcroft and N. D. Mermin, *Solid state physics* (Saunders College, Philadelphia, PA, USA, 1976).
[15] K. Nordlund and R. S. Averback, "Inverse kirkendall mixing in collision cascades," Phys. Rev. B **59**, 20–23 (1999).